

# Determination of Polypeptide Conformation with Nanoscale Resolution in Water

*Georg Ramer,<sup>[a,b]+</sup> Francesco Simone Ruggeri,<sup>[c]+</sup> Aviad Levin<sup>[c]</sup>, Tuomas P.J. Knowles<sup>[cd]</sup> & Andrea Centrone<sup>\*[a]</sup>*

[a] Center for Nanoscale Science and Technology, National Institute of Standards and Technology,  
Gaithersburg, Maryland 20899, United States

[b] Institute for Research in Electronics and Applied Physics, University of Maryland, College Park, MD  
20742, United States

[c] Department of Chemistry, University of Cambridge, Cambridge, United Kingdom, CB30FT

[d] Cavendish laboratory, Department of Physics, J J Thomson Avenue, CB3 1HE, Cambridge United  
Kingdom

**Corresponding author** E-mail: [andrea.centrone@nist.gov](mailto:andrea.centrone@nist.gov)

## **Abstract:**

The folding and acquisition of native structure of proteins is central to all biological processes of life. By contrast, protein misfolding can lead to toxic amyloid aggregates formation, linked to the onset of

neurodegenerative disorders. To shed light on the molecular basis of protein function and malfunction, it is crucial to access structural information of single protein assemblies and aggregates under native conditions. Yet, current conformation-sensitive spectroscopic methods lack the spatial resolution and sensitivity necessary for characterizing heterogeneous protein aggregates in solution. To overcome this limitation, here we use photothermal induced resonance (PTIR) to demonstrate that it is possible to acquire nanoscale infrared spectra in water with high signal to noise ratio (SNR). Using this approach, we probe supramolecular aggregates of diphenylalanine, the core recognition module of the Alzheimer's disease  $\beta$ -amyloid peptide, and its derivative Boc-diphenylalanine. We achieve nanoscale resolved IR spectra and maps in air and water with comparable SNR and lateral resolution, thus enabling accurate identification of the chemical and structural state of morphologically similar networks at the single aggregate (*i.e.* fibril) level.

Keywords: infrared nanospectroscopy, protein aggregation, PTIR, protein structure, AFM-IR

Proteins are central to essentially all molecular processes in living organisms, and typically carry out their activities by folding into a well-defined three-dimensional structure and by binding to other molecular species to form functional complexes. Several factors, however, including high temperature, high pressure, low pH, organic solvents and natural or post-translational mutations, can steer proteins to misfolding and promote their aberrant aggregation into amyloid fibrillar structures.<sup>1-6</sup> Through this misfolding process, specific peptides or proteins can lose their native functional conformational state and generate toxic aggregates, which are found at the core of a broad range of human diseases, including neurodegenerative disorders such as Alzheimer's disease.<sup>3</sup> The development of short peptide models that adopt amyloid-like structure through hydrophobic<sup>7</sup> and  $\pi$ - $\pi$  interactions<sup>8</sup> commonly found in amyloid structures, allow them to form supramolecular systems, which possess structural similarities to those found in amyloids. Among the wide range of self-assembling peptides, di-homopeptides, which can adopt amyloid-like fibrillar supramolecular structures, have been studied in great detail.<sup>9, 10</sup> Diphenylalanine, FF, the core recognition module of the Alzheimer's disease  $\beta$ -amyloid polypeptide, was shown to self-assemble into supramolecular systems and form nanotubes, nanospheres, nanofibrils, and hydrogels.<sup>8, 10, 11</sup> The formation of complex supramolecular polymers by such simple building blocks has been key for establishing FF as an archetypical model for the study of the self-assembly processes. This di-homopeptide and its analogues have allowed intense study into the mechanism underlying amyloid-related disorders propagation and their physical properties through studying their nucleation and polymerization pathway.<sup>12</sup> Several bulk techniques, such as Thioflavin T and Circular Dichroism have been developed to determine the structural properties of protein aggregates, yet these methods yield only average information, which is insufficient for characterizing the heterogeneous ensemble of species present in protein solutions.<sup>4, 13-15</sup>

Sensitive approaches for determining protein secondary and quaternary conformation and their aggregation are thus crucial to unravel their role in biological function and malfunction. An attractive

approach to determine proteins' compositional and structural information is infrared (IR) spectroscopy ensemble technique.<sup>16</sup> Recent advances in scanning probe techniques<sup>17-22</sup> have provided the ability to acquire IR spectra with nanoscale spatial resolution, which allows for the separation and determination of specific structural species in complex populations.<sup>23,24</sup> In particular, the photothermal induced resonance (PTIR) technique, also known as infrared nanospectroscopy (AFM-IR), has recently attracted much attention, due to the proportionality between the sample absorption coefficient and the PTIR signal,<sup>25-28</sup> along with the close agreement between nanoscale PTIR spectra and conventional far-field IR transmission spectra with a spatial resolution of  $\approx 20$  nm to  $\approx 50$  nm.<sup>21, 29</sup> These experiments have enabled nanoscale protein conformational analysis, allowing better understanding of the pathological amyloid fibrillar aggregation processes based on the determination of protein backbone conformation by the deconvolution of the conformation-sensitive Amide I band.<sup>20, 23, 28, 30, 31</sup> Similarly, such analysis has enabled the characterization of protein-based bio-scaffolds, carrier agents, estrogen receptors<sup>23, 24, 30, 32-34</sup> and of cataract diseased tissues.<sup>35</sup> Beyond biology, PTIR finds wide application in polymer science,<sup>36-38</sup> photovoltaics,<sup>39-40</sup> plasmonics,<sup>26, 41-43</sup> and pharmaceuticals.<sup>44</sup> Moreover, the PTIR mechanical detection scheme does not restrict this method to the IR and operation in the near-IR and visible ranges have been recently demonstrated.<sup>29, 39, 40</sup>

While PTIR has opened a nanoscale observation window on protein conformation in heterogeneous biological systems, there is a strong need to develop measurement approaches compatible with liquid environments, which can allow gathering information that is more physiologically relevant. Yet, PTIR measurement in water are challenging<sup>45</sup> due to the strong IR absorption background of water (from  $\approx 500$   $\text{cm}^{-1}$  to  $\approx 1750$   $\text{cm}^{-1}$ , and from  $\approx 2800$   $\text{cm}^{-1}$  to  $\approx 3800$   $\text{cm}^{-1}$ ) and because fluid drag dampens the atomic force microscopy (AFM) cantilever oscillations that yield the PTIR signal.

The first PTIR measurements in water<sup>45</sup> were obtained a decade ago for the *Candida Albicans* fungi with 1  $\mu\text{m}$  to 2  $\mu\text{m}$  thickness, by leveraging total internal reflection (TIR) illumination to minimize water direct

absorption. Only recently, a second set of PTIR experiments in liquid (D<sub>2</sub>O) was reported for polymethylmetacrylate (PMMA) samples with nanoscale thickness (20 nm to 50 nm).<sup>46</sup> Measuring such thin samples in liquid required a boost of the PTIR signal-to-noise ratio (SNR), which was achieved by resonantly exciting the AFM cantilever<sup>21</sup> and by nano-focusing the light in the sample volume confined between a Ge prism ( $n_{Ge} \approx 4.0$ ), and a gold coated probe.<sup>46</sup> Despite these sophisticated attempts, up to now, PTIR, and other nanoscale IR techniques, are considered not well suited for measurements in solution due to the low SNR achieved in practice ( $\approx 3.3$  and  $\approx 5$  for the thick fungi<sup>45</sup> and thin PMMA<sup>46</sup> samples, respectively), which is insufficient for reliable band deconvolution and secondary structure identification. Because thus far PTIR data in liquid have been obtained for samples where no nanoscale absorption heterogeneities were expected, the resulting PTIR maps were either correlated or anti-correlated with the sample topography.<sup>45, 46</sup>

Here, we show that PTIR spectra in aqueous solutions can be obtained with high SNR (up to  $> 70$ ). Furthermore, we demonstrate that PTIR maps and spectra on gold plasmonic resonators coated with a 200 nm thick PMMA layer are obtained in air and water with comparable SNR, lateral resolution and with a water absorption background that is comparatively weak with respect to the PMMA absorption. These samples were chosen as they are characterized by heterogeneous IR absorption at the nanoscale that is not correlated with their (flat) topography.<sup>26, 41</sup> We further leveraged PTIR spectra in water and D<sub>2</sub>O to detect peptide conformation on fibrillar supramolecular aggregates composed either by diphenylalanine (FF) or its tert-butoxycarbonyl (Boc)-modified derivative (Boc-FF) as model systems for amyloidogenic proteins. Along with being clinically relevant model compounds in the context of amyloid aggregation disorders, FF and Boc-FF have been chosen for this study as they yield fibrillar aggregates with similar morphology, whose different secondary structure cannot be inferred by morphology analysis alone. Thus, our results demonstrate the general capability to differentiate objects with similar morphology by their chemical and structural properties in liquid environment. We obtain IR spectra of individual nanoscale fibrillar aggregates in the

Amide I, II and III bands region (hereafter named protein fingerprint region) allowing chemical and structural identification of the FF fibrils in air, water and D<sub>2</sub>O. As these IR fingerprints, particularly the Amide band I, are related to the protein-backbone vibrations, they provide comprehensive insights into proteins secondary and quaternary structural properties. We successively measure structural differences between FF and Boc-FF fibrils, without the need for subtracting the water absorption background, thus demonstrating the ability to assess quantitatively subtle secondary and quaternary structural differences in proteins with PTIR in liquid.

## Results/Discussion

PTIR, also known as AFM-IR,<sup>17, 18</sup> leverages narrow-band wavelength-tunable pulsed lasers for sample excitation along with an AFM probe as a near-field mechanical detector (**Fig 1a**) to measure IR spectra and maps with sub 20 nm spatial resolution.<sup>21, 29</sup> Although PTIR setups that illuminate the sample from the air phase are common,<sup>18</sup> measurements in the liquid phase require sample illumination in total internal reflection (TIR) using an optical prism, ZnSe in this work, to curb the water absorption background. In PTIR, the AFM probe transduces the light-induced thermal expansion of the sample into cantilever oscillations that are detected by the AFM detector. Si<sub>3</sub>N<sub>4</sub> triangular AFM probes, without a metallic coating, were used in this work, demonstrating that high SNR is achievable in water even without resorting to the tip-induced field-enhancement typically provided by gold-coated probes. PTIR experiments in this work were obtained using s-polarized light, with the exception of the data reported in Figure S1.

PTIR absorption maps are obtained by scanning the AFM cantilever on the sample surface, while maintaining the laser wavelength fixed. Whereas, PTIR spectra are obtained by sweeping the laser wavelength maintaining the position of the AFM cantilever fixed. Through tuning of the PTIR laser repetition rate to match one of the cantilever oscillation frequencies, it is possible to increase the PTIR signal amplitude by the cantilever mode Q-factor,<sup>21</sup> which is very effective in air (high Q-factors),<sup>21</sup> as shown in **Fig 1b**. In

liquid, this mode of operation is key for obtaining PTIR data with sufficient SNR, although the fluid drag strongly dampens the AFM cantilever oscillations, thus reducing the Q-factors significantly (**Fig 1b**).

To demonstrate the ability of capturing high quality PTIR data in water we first obtained and compared data on an array made of gold asymmetric split ring resonators (ASSRs)<sup>26, 41, 42</sup> coated with 200 nm PMMA film either in air or in water (**Fig. 2**). We chose this sample for several reasons. First, previous extensive PTIR characterization in air have shown that similar samples exhibit spatially heterogeneous absorption at the nanoscale.<sup>26, 41, 42, 47</sup> Second, since the sample displays only small variations in thickness, the correlation between a spatially heterogeneous absorption and sample thickness (*i.e.* topography) can be excluded. Third, as the sample top layer is chemically homogenous, possible artefacts due to heterogeneity of the tip-sample mechanical contact<sup>48, 49</sup> (*i.e.* possible sensitivity of the PTIR signal to the sample mechanical properties) can be excluded. The ASSRs studied here have plasmon resonances of  $\approx 9 \mu\text{m}$  and were fabricated by electron-beam lithography and lift-off on a ZnSe prism.<sup>41</sup> The ASSRs have a diameter of  $1750 \text{ nm} \pm 50 \text{ nm}$ , thickness of  $180 \text{ nm} \pm 10 \text{ nm}$  and a pitch of  $3012 \text{ nm} \pm 22 \text{ nm}$ , as determined by AFM. After the deposition of the top PMMA layer, the sample shows an AFM maximum topographic variation of  $70 \text{ nm} \pm 10 \text{ nm}$ . The uncertainties throughout the manuscript represent a single standard deviation in the measurements on nominally identical resonators. The surface plasmon resonance (SPR) is a characteristic optical resonant response observed in noble metal nanostructures, which can be engineered by controlling the structure, composition size and shape.<sup>50, 51</sup> The nanoscale confinement of light, which promotes locally enhanced light-matter interactions is one of the most studied benefits provided by SPRs.<sup>41, 50-52</sup> For example, in the mid-IR, SPRs can be exploited for chemical identification by boosting the sensitivity of IR spectroscopy, an effect known as surface enhanced infrared absorption (SEIRA).<sup>26, 41, 50, 51, 53</sup> The AFM topography maps in air (**Fig 2a**) and water (**Fig 2b**) are quite similar and show the topographic outlines of the buried resonators and that the sample surface is rather flat. The PTIR maps (s-polarization  $1188 \text{ cm}^{-1}$ , corresponding to vibrations of

the ester group of PMMA) in air (**Fig 2c**) or water (**Fig 2d**) display the SEIRA enhancement (hot spots) arising from the field confinement near the resonators gaps.<sup>26, 41</sup> These images, obtained using a phase locked loop (PLL, see methods), demonstrate that PTIR imaging in water can be achieved without significant difference of resolution or SNR ( $\approx 17$  and  $\approx 35$  in air and water, respectively). Similar conclusions can be derived from the PTIR data obtained with p-polarization (see **Fig S1**). Although the lower Q-factors in water limit the effectiveness of the cantilever resonant excitation for amplifying the PTIR signal, they increase the bandwidth over which the PLL can effectively track the cantilever resonance, which is key for obtaining high quality images with this method. In **Fig. 2** the SNR of the PTIR image in water exceeds the one in air because the chosen AFM probe is well adapted to water operation and because of the broader bandwidth over which the PLL is effective in water. Representative PTIR spectra of PMMA obtained in the hot spot locations (**Fig 2e**), also display high SNR ( $235 \pm 13$  and  $70 \pm 7$  in air and water respectively). Comparison with the PMMA spectrum in water (**Fig 2e**), obtained away from the resonator, reveals SEIRA enhancement factors up to  $\approx 30$  in the hot-spot locations.

Having tested the PTIR capabilities in liquid on PMMA, we next characterize diphenylalanine (FF) supramolecular fibrillar aggregates as a model system to assess the capability to resolve chemical signatures and conformation of the polypeptide in water. FF, the core recognition module of the Alzheimer's disease  $\beta$ -amyloid polypeptide and its Boc modified analogue were shown to self-assemble into supramolecular systems and form a wide array of ordered structures,<sup>11, 54</sup> thus establishing FF as an archetypical model for the study of the fundamental principles governing the self-assembly process of proteins. In **Figure 3**, we show characteristic AFM morphology and PTIR absorption ( $1615\text{ cm}^{-1}$ ) maps of FF nanotubes with nanoscale diameter in air (**Fig.3a** and **SI Fig. 2**) and in water (**Fig.3b** and **SI Fig. 3**). The comparison of the IR maps in air and in water demonstrates that PTIR imaging in the liquid phase does not lead to a significant loss in spatial resolution, in agreement with the measurement on PMMA. PTIR spectra at selected locations



on the fibrillar samples cover the Amide I ( $1700\text{ cm}^{-1}$  to  $1600\text{ cm}^{-1}$ ), amide II ( $1580\text{ cm}^{-1}$  to  $1500\text{ cm}^{-1}$ ), to C-C ring vibrations and partially to Amide III ( $1500\text{ cm}^{-1}$  to  $1400\text{ cm}^{-1}$ ) regions both in air and in water (**SI Fig. 2-4**). As shown in **Fig. 3c**, the spectra in water and in air show a high degree of similarity along the whole protein fingerprint spectral range and match previous data reported in literature.<sup>55</sup> A more accurate comparison of the spectroscopic signatures can be obtained evaluating the second derivatives of the PTIR spectra (**Fig. 3d**). In the Amide band I region, both in water and in air, we can observe a sharp peak ( $1690\text{ cm}^{-1}$ ) that corresponds to antiparallel  $\beta$ -sheet conformation. The spectra present a slightly different shape between  $1640\text{ cm}^{-1}$  and  $1600\text{ cm}^{-1}$ , a variation that can be associated to changes in the hydration state of the  $\text{NH}_3^+$  groups (absorption at  $\approx 1600\text{ cm}^{-1}$ ) and to the presence of residual water absorption (between  $1640\text{ cm}^{-1}$  and  $1600\text{ cm}^{-1}$ ) within the nanotubes. The Amide II band shows absorption peaks at  $1555\text{ cm}^{-1}$  and  $1520\text{ cm}^{-1}$ . As the Amide II absorbance arises from NH vibrations, the small spectral differences in this region can be again related to the different hydration state of the sample when in air or liquid. Along with the amide bands, sharp bands associated to C-C ring vibrations at  $1605\text{ cm}^{-1}$ ,  $1495\text{ cm}^{-1}$ ,  $1452\text{ cm}^{-1}$  and  $1430\text{ cm}^{-1}$  are observed in the spectra. Due to the high quality PTIR data in water, the chemical signature and structural conformation of the FF fibrillar aggregates at the nanoscale can be determined with confidence. Similarly, it is possible to identify chemically and structurally the FF fibrils in liquid  $\text{D}_2\text{O}$  environment (**SI Fig. 4**). This is not surprising, as  $\text{D}_2\text{O}$  is commonly used to avoid spectral overlap between amide IR absorption bands and the  $\text{H}_2\text{O}$  absorption.

To assess further the PTIR capabilities in liquid, we focused on the Amide I vibrational signatures to investigate the structural differences between FF and Boc-FF nanotube aggregates (see AFM morphology in **Fig 4a-b**). The FF and the Boc-FF peptides chemical structures (**Fig. 4a-b**) only differ by the presence of the *tert*-butyloxycarbonyl group. To determine their secondary structure, and to rule out any possible influence related to the water absorption background on the conformational analysis due to partial spectral overlap, the

aggregates were formed in D<sub>2</sub>O. We could easily obtain chemical information from individual fibrillar aggregates with diameters smaller than 200 nm (SI Fig. 2, 5, 6). In Fig. 4c, we show the PTIR spectra comparison of the Amide band I region highlighting the different backbone structures of the two fibrillar aggregates. As expected based on the different chemical structure, spectra of the Boc-FF aggregates show an increased absorption at 1730 cm<sup>-1</sup> due to the additional carboxylic group with respect to the FF fibrils. Boc-FF also possesses a carbamate group absorbing at 1696 cm<sup>-1</sup>,<sup>55</sup> which overlaps with the antiparallel  $\beta$ -sheet absorption and contributes to a shift of the amide I band towards higher wavenumbers, thus justifying the different position of this structural-sensitive feature between Boc-FF and FF aggregates. Finally, as the presence of the *tert*-Butyloxycarbonyl group confers a larger conformational freedom with respect to FF, the Boc-FF fibrils spectrum exhibits an additional amide I contribution (1664 cm<sup>-1</sup> to 1655 cm<sup>-1</sup>), that is related to the  $\alpha$ -helix and 3-helix conformations. This analysis was confirmed by the observation of the second derivatives of the spectra (Fig 4d).

## Conclusions

To conclude, we demonstrate the identification of the chemical signature of individual fibrillar aggregates measured in water at the nanoscale, enabling the determination and comparison of their secondary structural conformation. Our data confirm that the FF and Boc-FF fibrils differ structurally at the individual fibril level due to the presence of  $\alpha$ -helical conformation of the Boc-FF with respect to the pure  $\beta$ -sheet conformation of FF. This highly sensitive and nanoscale-resolved characterization can thus be further applied for studies of more complex aggregating systems in water. We believe that the development of advanced biophysical methodologies, capable of bridging morphological and structural properties investigations of amyloid-like aggregates at the nanoscale, represents a fruitful avenue to address the challenges of fully

understanding protein self-assembly, to unravel monomer misfolding and to elucidate the molecular mechanisms of neurodegeneration. Furthermore, as an ever-growing class of functional amyloids has been recently found to occur naturally in disease-unrelated biological processes and as many artificial peptides can form amyloid-like structures *in-vitro*, we believe this work will influence protein research in a broad set of applications. Finally, recently introduced nano-sized AFM probes leveraging integrated cavity optomechanics that yield significantly increased PTIR sensitivity, time resolution and throughput,<sup>22</sup> hold further promise for an improved PTIR performance in liquid thanks to a much reduced cantilever drag.

## Methods/Experimental

PTIR sample preparation and deposition. H-L-Phe-L-Phe-COOH (FF) was dissolved in H<sub>2</sub>O and D<sub>2</sub>O at a concentration of 1 mg/ml to form supramolecular aggregates as previously reported.<sup>56</sup> N-(tert-butoxycarbonyl)-L-Phe-L-Phe-COOH (Boc-FF) stock solutions at a concentration of 10 mg/ml were prepared in absolute EtOH and then diluted at a ratio of 1:10 in H<sub>2</sub>O and D<sub>2</sub>O to allow formation of aggregates as previously reported.<sup>11</sup> An aliquot of each sample was deposit on a hydrophobic ZnSe prism for further analysis.<sup>23, 57</sup>

PTIR data acquisition. A modified commercial PTIR setup<sup>29</sup> using TIR illumination and interfaced with an external-cavity quantum cascade laser (EC-QCL) array covering the spectral range from 769 cm<sup>-1</sup> to 1763 cm<sup>-1</sup> was used for the PTIR experiments. The repetition rate of the EC-QCL source (tunable between 0.1 kHz and 2000 kHz) was set to match one of the cantilever oscillation mode in air or liquid (see fig 1b) to resonantly exciting the AFM cantilever (resonance-enhanced PTIR).<sup>21</sup> For imaging a phase locked loop (PLL) was used to maintain the contact resonance excitation condition throughout the measurement. The samples were deposited from solution onto right angle ZnSe prism substrates. Triangular Si<sub>3</sub>N<sub>4</sub> cantilevers with a nominal

length of  $120\ \mu\text{m} \pm 5\ \mu\text{m}$  and a first resonance frequency (non-contact in air) of  $65\ \text{kHz} \pm 15\ \text{kHz}$ , were used in the PTIR experiments. After deposition, the sample solution was replenished with a syringe filled with either  $\text{H}_2\text{O}$  or  $\text{D}_2\text{O}$  as needed. In the experiments both the sample and the AFM cantilever were completely immersed in the liquid. The PTIR instrument was operated in ambient atmosphere without precautions to prevent hydrogen-deuterium exchange of the liquid phase with ambient humidity during the measurement. PTIR data analysis. PTIR spectra on PMMA are averages of 5 single spectra taken at the same location. No further data processing was performed. The SNR in the PTIR spectra was determined as the ratio of the PTIR intensity at  $1160\ \text{cm}^{-1}$  and the standard deviation of the PTIR signal in the range between  $1510\ \text{cm}^{-1}$  and  $1560\ \text{cm}^{-1}$  where the PMMA spectrum is typically flat. The uncertainties of the SNR were calculated as the standard deviation of the SNRs of five spectra measured under the same conditions. The SEIRA enhancement was determined as the ratio of the PTIR intensity at the hotspot locations with respect to the intensity of the PTIR spectrum away from the resonators. Before calculating the ratio, five PTIR spectra were averaged and then smoothed, using a finite impulse response digital filter.

The SNR in PTIR images of the plasmonic resonators was determined as the ratio of the maximum PTIR amplitude value and the standard deviation of the PTIR amplitude away from the hotspots.

The spectra of the peptides were processed first by averaging at least 10 nominally identical spectra obtained in a given sample position. To remove the water contribution from the FF spectra, a reference spectrum was obtained with the AFM in contact with the substrate (water background spectrum). The two spectra are first normalized to their maximum intensities and then either subtracted or divided leading to similar results (SI Fig. 3). Later the spectra were smoothed by adjacent averaging (3 points) Savitzky-Golay filter (2<sup>nd</sup> order, 12 points) and finally their maximum intensities were normalised to one for comparison. For band deconvolution, second derivative spectra (2<sup>nd</sup> order, 9 points) were calculated from the normalized spectra. All these operations were carried out in a commercial statistics software package.

## **ASSOCIATED CONTENT**

### **Supporting information**

The Supporting Information is available free of charge on the ACS Publications website at

Additional information includes: PTIR measurement on PMMA coated plasmonic resonators with p-polarization, PTIR spectra of FF fibrils in air H<sub>2</sub>O and D<sub>2</sub>O, PTIR spectra of Boc-FF fibrils in D<sub>2</sub>O.

## **AUTHOR INFORMATION**

### **Corresponding author**

\*Dr. A. Centrone, Center for Nanoscale Science and Technology, National Institute of Standards and Technology, Gaithersburg, Maryland 20899, United States, E-mail: [andrea.centrone@nist.gov](mailto:andrea.centrone@nist.gov)

### **Author Contributions**

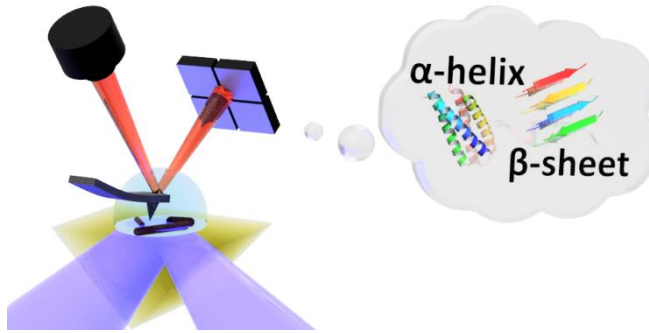
The manuscript was written through contributions of all authors. All authors have given approval to the final version of the manuscript.

<sup>+</sup> These authors contributed equally.

## **ACKNOWLEDGEMENTS**

GR acknowledges support under the Cooperative Research Agreement between the University of Maryland and the National Institute of Standards and Technology Center for Nanoscale Science and Technology, Award 70NANB14H209, through the University of Maryland. This work is supported by the Swiss National Science Foundation (F.S.R., grant number P2ELP2\_162116 & P300P2\_171219).

TOC



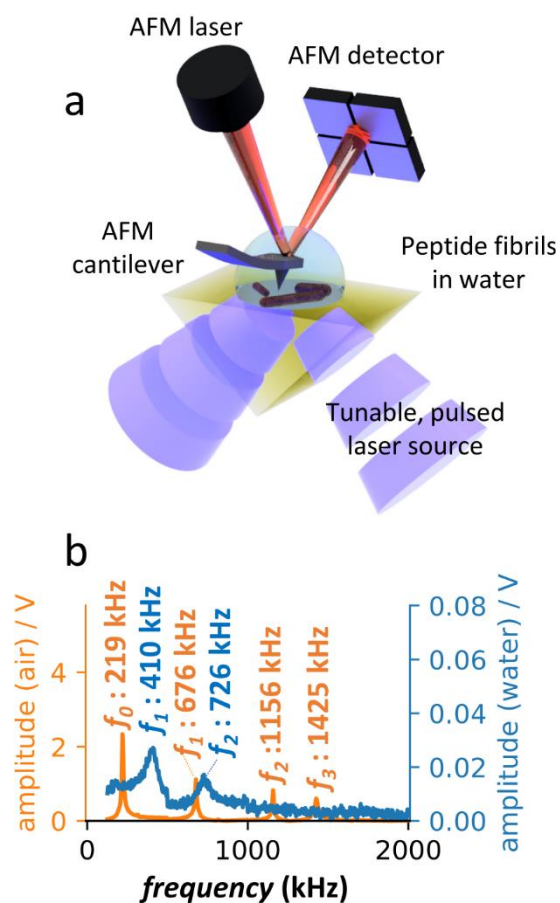


**Figure 1. PTIR set up in water.** a) PTIR measurement schematic. The sample is illuminated from below in TIR configuration. The AFM cantilever transduces the photo-induced thermal expansion of the sample as measured by the AFM detector. b) AFM cantilever contact resonant frequencies in air (orange) and water (blue).

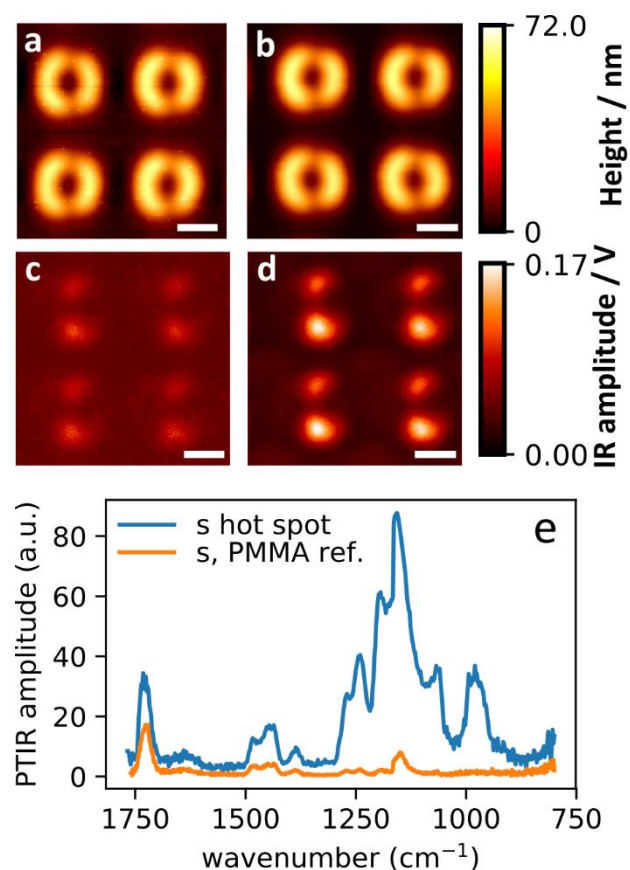


**Figure 2. Comparison of PTIR measurement in air and water.** AFM topography images of gold plasmonic resonators coated with 200 nm PMMA layer in air (a) and water (b). Corresponding PTIR absorption images ( $1188\text{ cm}^{-1}$ ) in air (c) and water (d). All images were obtained using s-polarized light. All scale bars are  $1.0\text{ }\mu\text{m}$  (e) Comparison of representative PTIR spectra in water obtained from a hotspot location and on the PMMA film away from the resonator (reference).



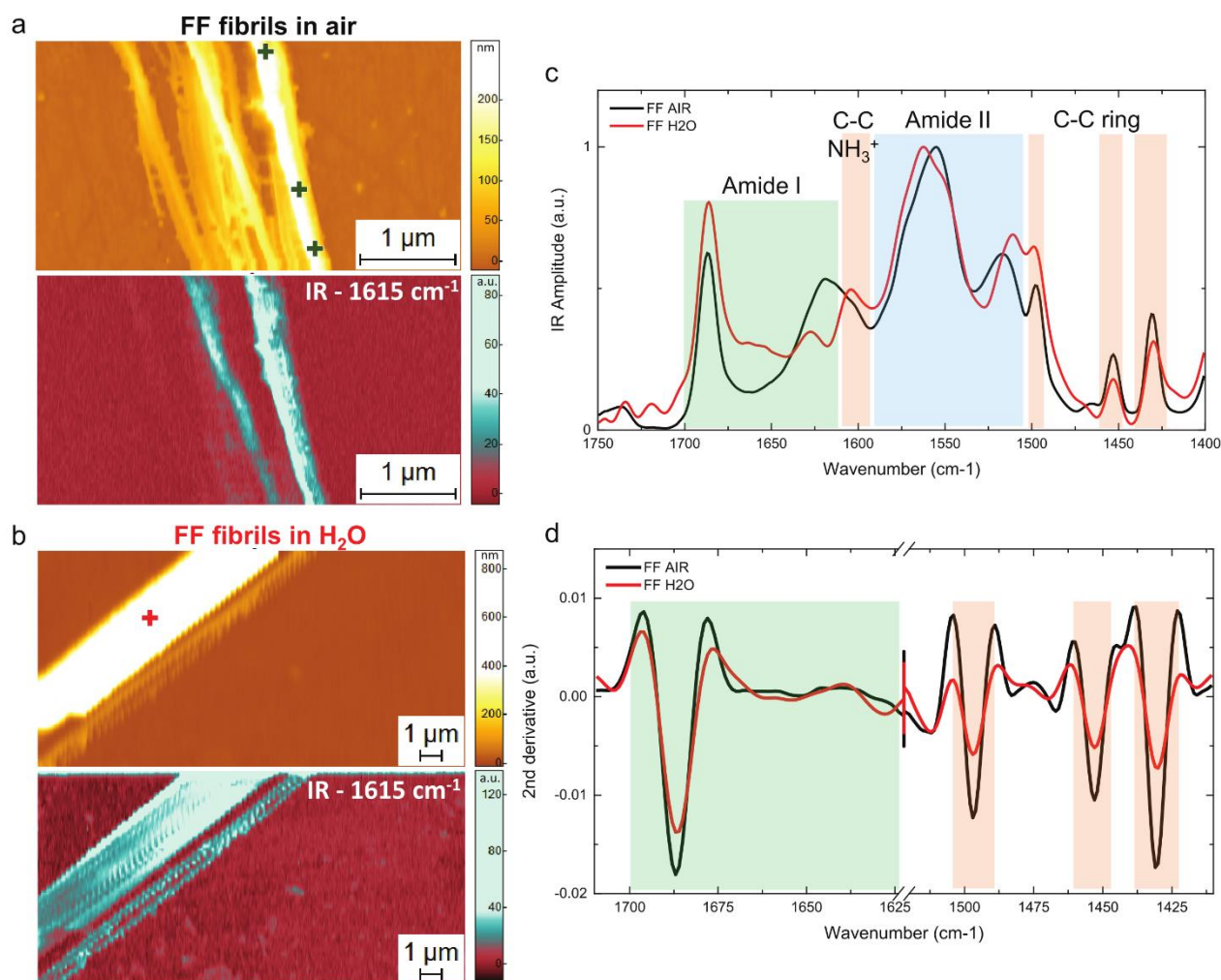


**Figure 3. PTIR measurement of FF fibrils in air and  $\text{H}_2\text{O}$ .** Morphology and IR absorption map (1615  $\text{cm}^{-1}$ ) for FF fibrils in a) air and b)  $\text{H}_2\text{O}$ . c) Comparison of the average PTIR spectra covering the Amide I band (green), amide II (blue) and C-C ring (orange) spectral regions. The + symbols mark the locations where the individual spectra reported in the SI Figs 2-3 where acquired. d) Comparison of the second derivatives of the spectra in the Amide band I and C-C ring absorption.

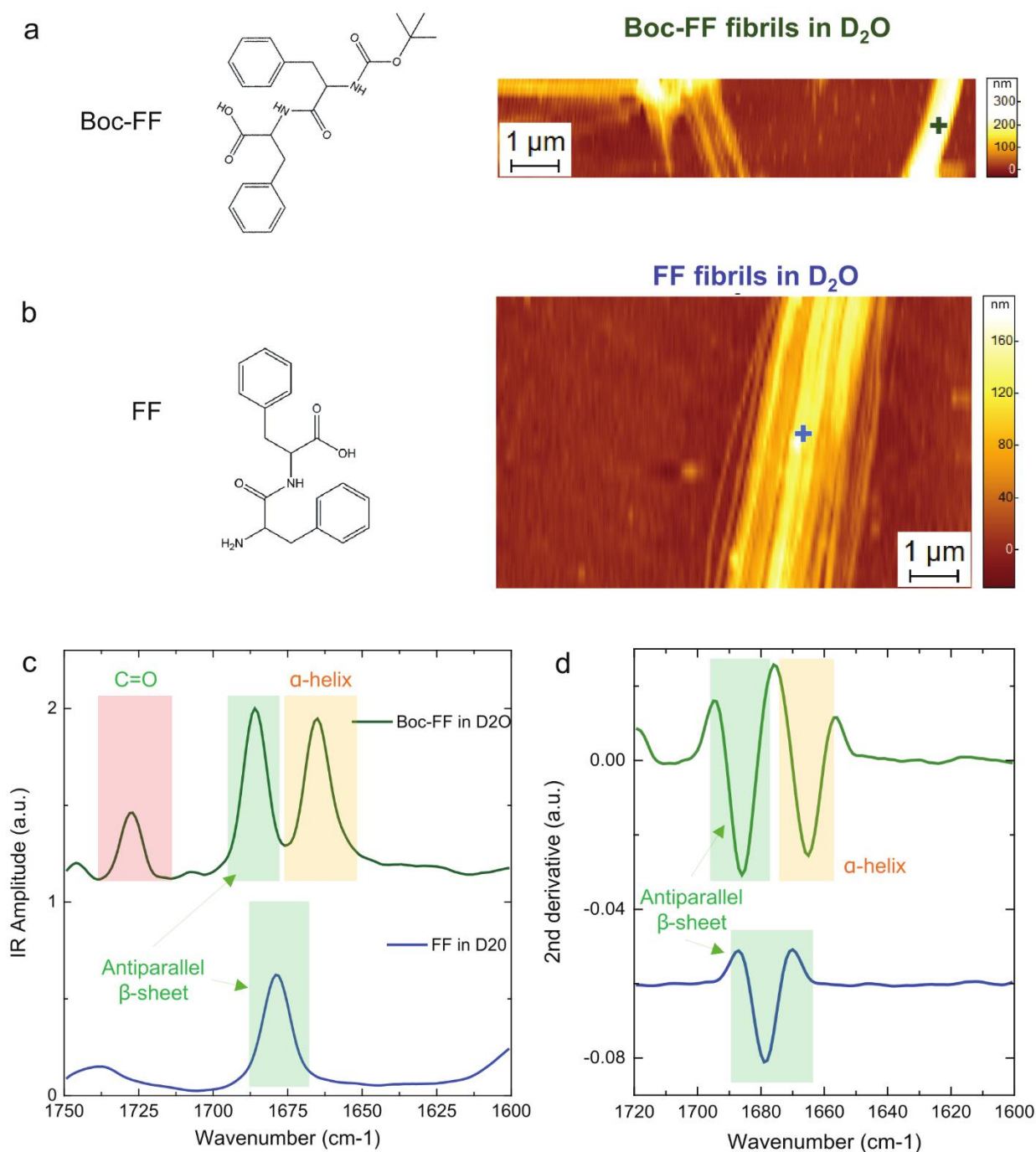


**Figure 4. PTIR structural comparison of FF and Boc-FF fibrils in D<sub>2</sub>O.** Chemical structure and AFM morphology map of a) Boc-FF and b) FF fibrils. c) Comparison of the fibrils average PTIR spectra in the Amide I (green and yellow) and C=O stretching vibration (red) spectral ranges. The + symbols mark the locations of the individually acquired spectra, reported in SI Fig. 2-3. d) Comparison of the second derivatives spectra in the Amide band I region.

## REFERENCES

1. Chiti, F.; Dobson, C. M., Protein Misfolding, Functional Amyloid, and Human Disease. *Annu. Rev. Biochem.* **2006**, *75*, 333-366.
2. Dobson, C. M., Protein Folding and Misfolding. *Nature* **2003**, *426*, 884-890.
3. Knowles, T. P. J.; Vendruscolo, M.; Dobson, C. M., The Amyloid State and Its Association with Protein Misfolding Diseases. *Nat. Rev. Mol. Cell Biol.* **2014**, *15*, 384-396.
4. Stefani, M.; Dobson, C. M., Protein Aggregation and Aggregate Toxicity: New Insights into Protein Folding, Misfolding Diseases and Biological Evolution. *J. Mol. Med.* **2003**, *81*, 678-699.
5. Soto, C., Unfolding the Role of Protein Misfolding in Neurodegenerative Diseases. *Nat. Rev. Neurosci.* **2003**, *4*, 49-60.
6. Dobson, C. M., Protein Misfolding, Evolution and Disease. *Trends Biochem. Sci.* **1999**, *24*, 329-332.
7. Mart, R. J.; Osborne, R. D.; Stevens, M. M.; Ulijn, R. V., Peptide-Based Stimuli-Responsive Biomaterials. *Soft Matter* **2006**, *2*, 822-835.
8. Orbach, R.; Mironi-Harpaz, I.; Adler-Abramovich, L.; Mossou, E.; Mitchell, E. P.; Forsyth, V. T.; Gazit, E.; Seliktar, D., The Rheological and Structural Properties of Fmoc-Peptide-Based Hydrogels: The Effect of Aromatic Molecular Architecture on Self-Assembly and Physical Characteristics. *Langmuir* **2012**, *28*, 2015-2022.
9. Gazit, E., A Possible Role for Pi-Stacking in the Self-Assembly of Amyloid Fibrils. *FASEB J.* **2002**, *16*, 77-83.
10. Reches, M.; Gazit, E., Designed Aromatic Homo-Dipeptides: Formation of Ordered Nanostructures and Potential Nanotechnological Applications. *Phys. Biol.* **2006**, *3*, S10-S19.
11. Levin, A.; Mason, T. O.; Adler-Abramovich, L.; Buell, A. K.; Meisl, G.; Galvagnion, C.; Bram, Y.; Stratford, S. A.; Dobson, C. M.; Knowles, T. P.; Gazit, E., Ostwald's Rule of Stages Governs Structural Transitions and Morphology of Dipeptide Supramolecular Polymers. *Nat. Commun.* **2014**, *5*, 5219.
12. Mason, T. O.; Michaels, T. C. T.; Levin, A.; Dobson, C. M.; Gazit, E.; Knowles, T. P. J.; Buell, A. K., Thermodynamics of Polypeptide Supramolecular Assembly in the Short-Chain Limit. *J. Am. Chem. Soc.* **2017**, *139*, 16134-16142.
13. Ruggeri, F. S.; Adamcik, J.; Jeong, J. S.; Lashuel, H. A.; Mezzenga, R.; Dietler, G., Influence of the B-Sheet Content on the Mechanical Properties of Aggregates During Amyloid Fibrillization. *Angew. Chem., Int. Ed.* **2015**, *127*, 2492-2496.
14. Zandomenighi, G.; Krebs, M. R.; McCammon, M. G.; Fandrich, M., FTIR Reveals Structural Differences between Native Beta-Sheet Proteins and Amyloid Fibrils. *Protein Sci.* **2004**, *13*, 3314-21.
15. Whitmore, L.; Wallace, B. A., Protein Secondary Structure Analyses from Circular Dichroism Spectroscopy: Methods and Reference Databases. *Biopolymers* **2008**, *89*, 392-400.
16. Barth, A., Infrared Spectroscopy of Proteins. *Biochim. Biophys. Acta, Bioenerg.* **2007**, *1767*, 1073-101.
17. Centrone, A., Infrared Imaging and Spectroscopy Beyond the Diffraction Limit. *Annu. Rev. Anal. Chem.* **2015**, *8*, 101-126.
18. Dazzi, A.; Prater, C. B., AFM-IR: Technology and Applications in Nanoscale Infrared Spectroscopy and Chemical Imaging. *Chem. Rev.* **2017**, *117*, 5146-5173.
19. Xiao, L.; Schultz, Z. D., Spectroscopic Imaging at the Nanoscale: Technologies and Recent Applications. *Anal. Chem.* **2017**, *90*, 440-458.
20. Ruggeri, F. S.; Habchi, J.; Cerreta, A.; Dietler, G., AFM-Based Single Molecule Techniques: Unraveling the Amyloid Pathogenic Species. *Curr. Pharm. Des.* **2016**, *22*, 3950-3970.
21. Lu, F.; Jin, M. Z.; Belkin, M. A., Tip-Enhanced Infrared Nanospectroscopy Via Molecular Expansion Force Detection. *Nat. Photonics* **2014**, *8*, 307-312.
22. Chae, J.; An, S.; Ramer, G.; Stavila, V.; Holland, G.; Yoon, Y.; Talin, A. A.; Allendorf, M.; Aksyuk, V. A.; Centrone, A., Nanophotonic Atomic Force Microscope Transducers Enable Chemical Composition and Thermal Conductivity Measurements at the Nanoscale. *Nano Lett.* **2017**, *17*, 5587-5594.
23. Ruggeri, F. S.; Longo, G.; Faggiano, S.; Lipiec, E.; Pastore, A.; Dietler, G., Infrared Nanospectroscopy Characterization of Oligomeric and Fibrillar Aggregates During Amyloid Formation. *Nat. Commun.* **2015**, *6*, 7831.

24. Galante, D.; Ruggeri, F. S.; Dietler, G.; Pellistri, F.; Gatta, E.; Corsaro, A.; Florio, T.; Perico, A.; D'Arrigo, C., A Critical Concentration of N-Terminal Pyroglutamylated Amyloid Beta Drives the Misfolding of Ab1-42 into More Toxic Aggregates. *Int. J. Biochem. Cell Biol.* **2016**, *79*, 261-270.
25. Dazzi, A.; Glotin, F.; Carminati, R., Theory of Infrared Nanospectroscopy by Photothermal Induced Resonance. *J. Appl. Phys.* **2010**, *107*, 124519.
26. Lahiri, B.; Holland, G.; Aksyuk, V.; Centrone, A., Nanoscale Imaging of Plasmonic Hot Spots and Dark Modes with the Photothermal-Induced Resonance Technique. *Nano Lett.* **2013**, *13*, 3218-3224.
27. Tang, F.; Bao, P.; Su, Z., Analysis of Nanodomain Composition in High-Impact Polypropylene by Atomic Force Microscopy-Infrared. *Anal. Chem.* **2016**, *88*, 4926-4930.
28. Ramer, G.; Aksyuk, V. A.; Centrone, A., Quantitative Chemical Analysis at the Nanoscale Using the Photothermal Induced Resonance Technique. *Anal. Chem.* **2017**, *89*, 13524-13531.
29. Katzenmeyer, A. M.; Holland, G.; Kjoller, K.; Centrone, A., Absorption Spectroscopy and Imaging from the Visible through Mid-Infrared with 20 nm Resolution. *Anal. Chem.* **2015**, *87*, 3154-3159.
30. Ruggeri, F. S.; Vieweg, S.; Cendrowska, U.; Longo, G.; Chiki, A.; Lashuel, H. A.; Dietler, G., Nanoscale Studies Link Amyloid Maturity with Polyglutamine Diseases Onset. *Sci. Rep.* **2016**, *6*, 31155.
31. Qamar, S.; Wang, G.; Randle, S. J.; Ruggeri, F. S.; Varela, J. A.; Lin, J. Q.; Phillips, E. C.; Miyashita, A.; Williams, D.; Strohl, F.; Meadows, W.; Ferry, R.; Dardov, V. J.; Tartaglia, G. G.; Farrer, L. A.; Kaminski Schierle, G. S.; Kaminski, C. F.; Holt, C. E.; Fraser, P. E.; Schmitt-Ulms, G., *et al.*, Fus Phase Separation Is Modulated by a Molecular Chaperone and Methylation of Arginine Cation- $\pi$  Interactions. *Cell* **2018**, *173*, 720-734 e15.
32. Muller, T.; Ruggeri, F. S.; Kulik, A. J.; Shimanovich, U.; Mason, T. O.; Knowles, T. P. J.; Dietler, G., Nanoscale Spatially Resolved Infrared Spectra from Single Microdroplets. *Lab Chip* **2014**, *14*, 1315-1319.
33. Ruggeri, F. S.; Byrne, C.; Khemtouri, L.; Ducouret, G.; Dietler, G.; Jacquot, Y., Concentration-Dependent and Surface-Assisted Self-Assembly Properties of a Bioactive Estrogen Receptor Alpha-Derived Peptide. *J. Pept. Sci.* **2015**, *21*, 95-104.
34. Volpatti, L. R.; Shimanovich, U.; Ruggeri, F. S.; Bolisetty, S.; Muller, T.; Mason, T. O.; Michaels, T. C. T.; Mezzenga, R.; Dietler, G.; Knowles, T. P. J., Micro- and Nanoscale Hierarchical Structure of Core-Shell Protein Microgels. *J. Mater. Chem. B* **2016**, *4*, 7989-7999.
35. Paluszkiwicz, C.; Piergies, N.; Chaniecki, P.; Rekas, M.; Mischczyk, J.; Kwiatek, W. M., Differentiation of Protein Secondary Structure in Clear and Opaque Human Lenses: AFM - IR Studies. *J. Pharm. Biomed. Anal.* **2017**, *139*, 125-132.
36. Gong, L.; Chase, D. B.; Noda, I.; Marcott, C. A.; Liu, J.; Martin, D. C.; Ni, C.; Rabolt, J. F., Polymorphic Distribution in Individual Electrospun Poly[(R)-3-Hydroxybutyrate-Co-(R)-3-Hydroxyhexanoate] (Phbhx) Nanofibers. *Macromolecules* **2017**, *50*, 5510-5517.
37. Morsch, S.; Liu, Y. W.; Lyon, S. B.; Gibbon, S. R., Insights into Epoxy Network Nanostructural Heterogeneity Using AFM-IR. *ACS Appl. Mater. Interfaces* **2016**, *8*, 959-966.
38. Tri, P. N.; Prud'homme, R. E., Nanoscale Lamellar Assembly and Segregation Mechanism of Poly(3-Hydroxybutyrate)/Poly(Ethylene Glycol) Blends. *Macromolecules* **2018**, *51*, 181-188.
39. Strelcov, E.; Dong, Q.; Li, T.; Chae, J.; Shao, Y.; Deng, Y.; Gruverman, A.; Huang, J.; Centrone, A., Ch<sub>3</sub>Nh<sub>3</sub>PbI<sub>3</sub> Perovskites: Ferroelasticity Revealed. *Sci. Adv.* **2017**, *3*, e1602165.
40. Chae, J.; Dong, Q.; Huang, J.; Centrone, A., Chloride Incorporation Process in Ch(3)Nh(3)Pbi(3-X)Cl(X) Perovskites Via Nanoscale Bandgap Maps. *Nano Lett.* **2015**, *15*, 8114-8121.
41. Chae, J.; Lahiri, B.; Centrone, A., Engineering near-Field SEIRA Enhancements in Plasmonic Resonators. *ACS Photonics* **2016**, *3*, 87-95.
42. Katzenmeyer, A. M.; Chae, J.; Kasica, R.; Holland, G.; Lahiri, B.; Centrone, A., Nanoscale Imaging and Spectroscopy of Plasmonic Modes with the PTIR Technique. *Adv. Opt. Mater.* **2014**, *2*, 718-722.
43. Khanikaev, A. B.; Arju, N.; Fan, Z.; Purtseladze, D.; Lu, F.; Lee, J.; Sarriugarte, P.; Schnell, M.; Hillenbrand, R.; Belkin, M. A.; Shvets, G., Experimental Demonstration of the Microscopic Origin of Circular Dichroism in Two-Dimensional Metamaterials. *Nat. Commun.* **2016**, *7*, 12045.
44. Van Eerdenbrugh, B.; Lo, M.; Kjoller, K.; Marcott, C.; Taylor, L. S., Nanoscale Mid-Infrared Imaging of Phase Separation in a Drug-Polymer Blend. *J. Pharm. Sci.* **2012**, *101*, 2066-2073.

45. Mayet, C.; Dazzi, A.; Prazeres, R.; Allot, E.; Glotin, E.; Ortega, J. M., Sub-100 nm IR Spectromicroscopy of Living Cells. *Opt. Lett.* **2008**, *33*, 1611-1613.
46. Jin, M.; Lu, F.; Belkin, M. A., High-Sensitivity Infrared Vibrational Nanospectroscopy in Water. *Light: Sci. Appl.* **2017**, *6*, e17096.
47. Chae, J.; Lahiri, B.; Kohoutek, J.; Holland, G.; Lezec, H.; Centrone, A., Metal-Dielectric-Metal Resonators with Deep Subwavelength Dielectric Layers Increase the near-Field SEIRA Enhancement. *Opt. Express* **2015**, *23*, 25912-25922.
48. Barlow, D. E.; Biffinger, J. C.; Cockrell-Zugell, A. L.; Lo, M.; Kjoller, K.; Cook, D.; Lee, W. K.; Pehrsson, P. E.; Crookes-Goodson, W. J.; Hung, C. S.; Nadeau, L. J.; Russell, J. N., The Importance of Correcting for Variable Probe-Sample Interactions in AFM-IR Spectroscopy: AFM-IR of Dried Bacteria on a Polyurethane Film. *Analyst* **2016**, *141*, 4848-4854.
49. Ramer, G.; Reisenbauer, F.; Steindl, B.; Tomischko, W.; Lendl, B., Implementation of Resonance Tracking for Assuring Reliability in Resonance Enhanced Photothermal Infrared Spectroscopy and Imaging. *Appl. Spec.* **2017**, *71*, 2013-2020.
50. Mayerhofer, T. G.; Popp, J., Periodic Array-Based Substrates for Surfaceenhanced Infrared Spectroscopy. *Nanophotonics* **2018**, *7*, 39-79.
51. Neubrech, F.; Huck, C.; Weber, K.; Pucci, A.; Giessen, H., Surface-Enhanced Infrared Spectroscopy Using Resonant Nanoantennas. *Chem. Rev.* **2017**, *117*, 5110-5145.
52. Bailo, E.; Deckert, V., Tip-Enhanced Raman Scattering. *Chem. Soc. Rev.* **2008**, *37*, 921-930.
53. Etezadi, D.; Warner IV, J. B.; Ruggeri, F. S.; Dietler, G.; Lashuel, H. A.; Altug, H., Nanoplasmonic Mid-Infrared Biosensor for *in Vitro* Protein Secondary Structure Detection. *Light: Sci. Appl.* **2017**, *6*, e17029.
54. Reches, M.; Gazit, E., Self-Assembly of Peptide Nanotubes and Amyloid-Like Structures by Charged-Termini-Capped Diphenylalanine Peptide Analogues. *Isr. J. Chem.* **2005**, *45*, 363-371.
55. Creasey, R. C. G.; Louzao, I.; Arnon, Z. A.; Marco, P.; Adler-Abramovich, L.; Roberts, C. J.; Gazit, E.; Tendler, S. J. B., Disruption of Diphenylalanine Assembly by a Boc-Modified Variant. *Soft Matter* **2016**, *12*, 9451-9457.
56. Mason, T. O.; Chirgadze, D. Y.; Levin, A.; Adler-Abramovich, L.; Gazit, E.; Knowles, T. P.; Buell, A. K., Expanding the Solvent Chemical Space for Self-Assembly of Dipeptide Nanostructures. *ACS Nano* **2014**, *8*, 1243-1253.
57. Jeon, J. S.; Raghavan, S.; Sperline, R. P., Quantitative Analysis of Albumin Adsorption onto Uncoated and Poly(Ether)Urethane-Coated Znse Surfaces Using the Attenuated Total Reflection FTIR Technique. *Colloids Surf., A* **1994**, *92*, 255-265.

Supporting information for:

# Determination of Polypeptide Conformation with Nanoscale Resolution in Water

*Georg Ramer,<sup>[a,b]</sup>+ Francesco Simone Ruggeri,<sup>[c]</sup>+ Aviad Levin<sup>[c]</sup>, Tuomas P.J. Knowles<sup>[cd]</sup> & Andrea Centrone<sup>\*[a]</sup>*

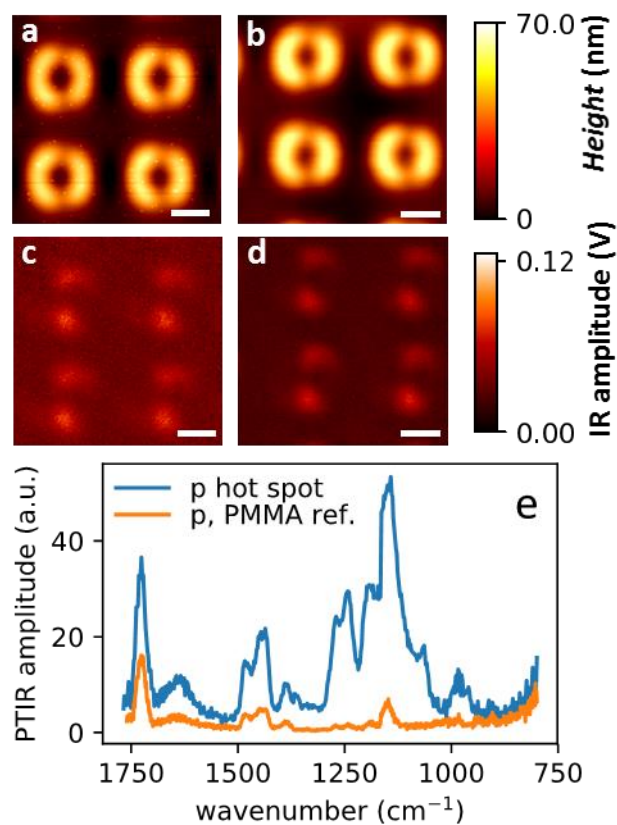
[a] Center for Nanoscale Science and Technology, National Institute of Standards and Technology,  
Gaithersburg, Maryland 20899, United States

[b] Maryland Nanocenter, University of Maryland, College Park, Maryland 20742

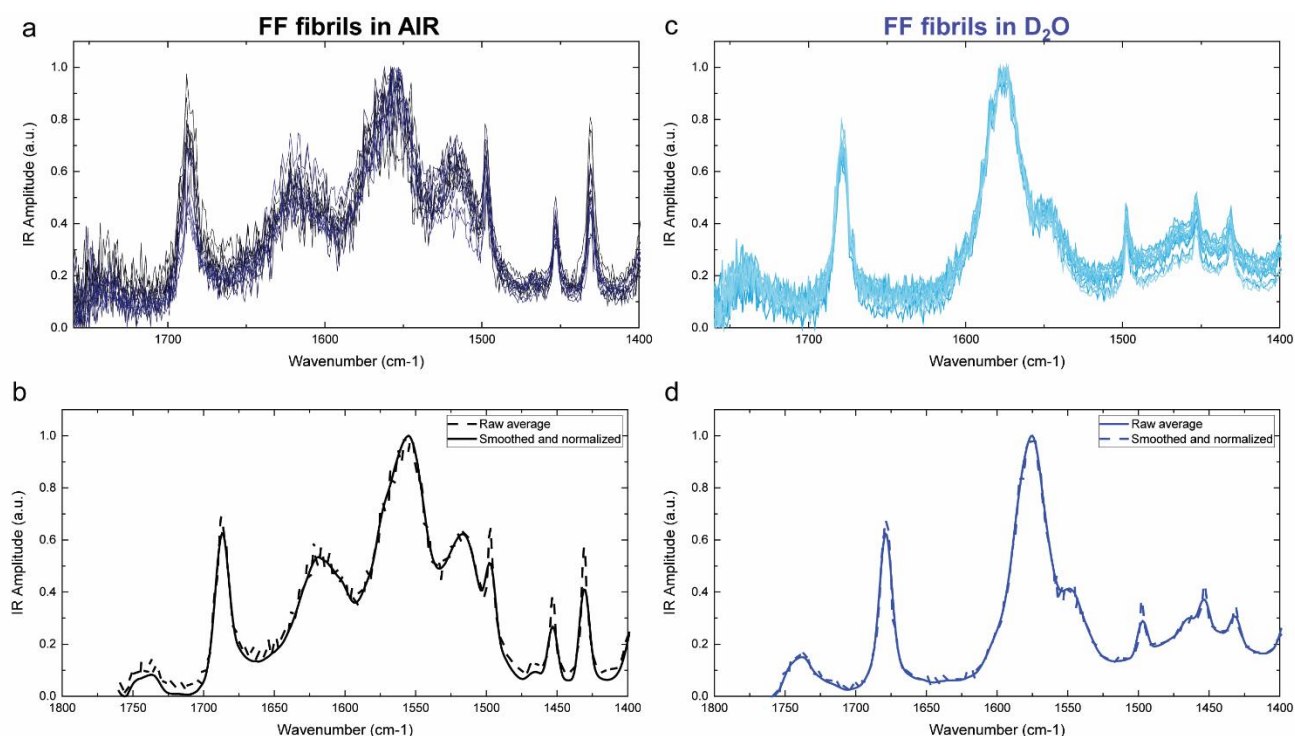
[c] Department of Chemistry, University of Cambridge, Cambridge, United Kingdom, CB30FT

[d] Cavendish laboratory, Department of Physics, J J Thomson Avenue, CB3 1HE, Cambridge United  
Kingdom

+ These authors equally contributed.

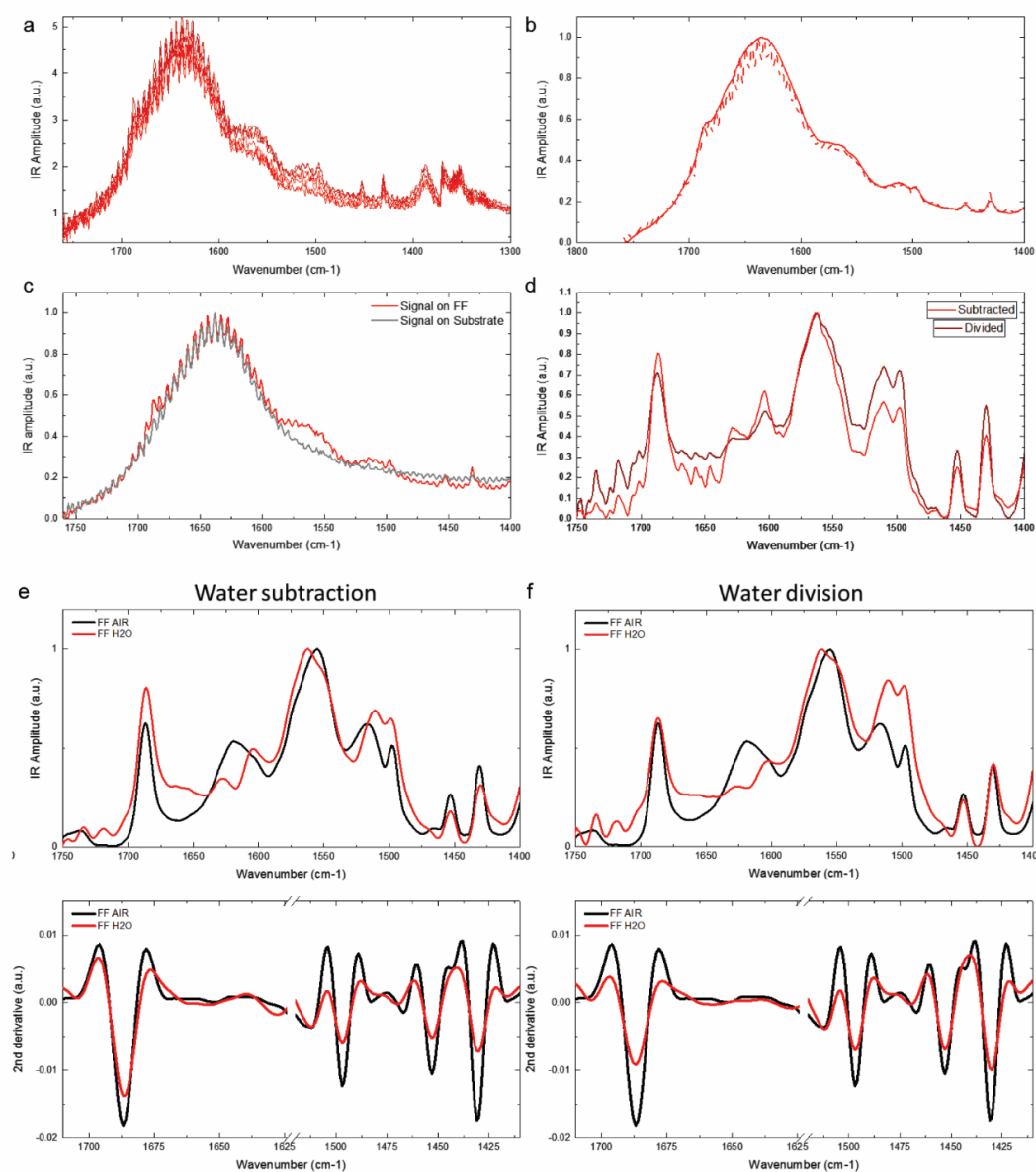


**Supplementary Figure 1. PTIR measurements with p-polarized light.** Topography images of gold plasmonic resonators coated with 200 nm PMMA layer in air (a) and water (b). Corresponding PTIR absorption maps at  $1188\text{ cm}^{-1}$  of resonators in air (c) and water (d). All images were obtained using light with p-polarization. All scale bars are  $1.0\text{ }\mu\text{m}$ . (e) Comparison of representative PTIR spectra in water obtained from a hotspot location and on the PMMA film away from the resonator (reference).



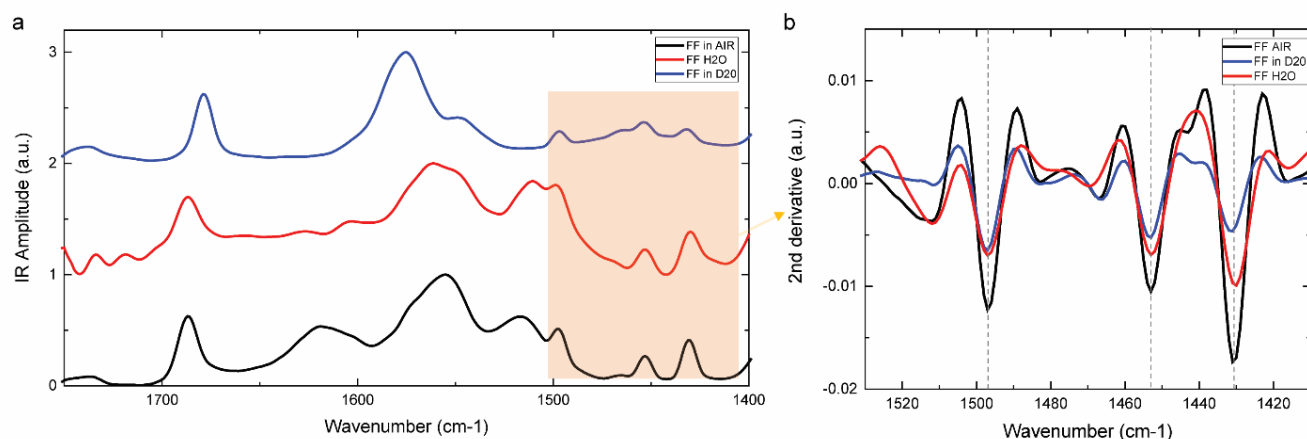
**Supplementary Figure 2. PTIR spectra of FF fibrils in air and D<sub>2</sub>O.** a) As recorded, b) averaged (dotted line) and smoothed (full line) PTIR absorption spectra obtained from the FF fibrils in air. The as recorded spectra in a) were obtained from the 3 locations indicated by the blue crosses on the FF fibril in Fig. 3a; while the average spectrum in b) derives from the average of all the spectra acquired at the 3 positions. c) As recorded, d) averaged (dotted line) and, smoothed (full line) PTIR absorption spectra obtained in D<sub>2</sub>O from position on the FF fibril marked by the blue cross in Fig. 4b.



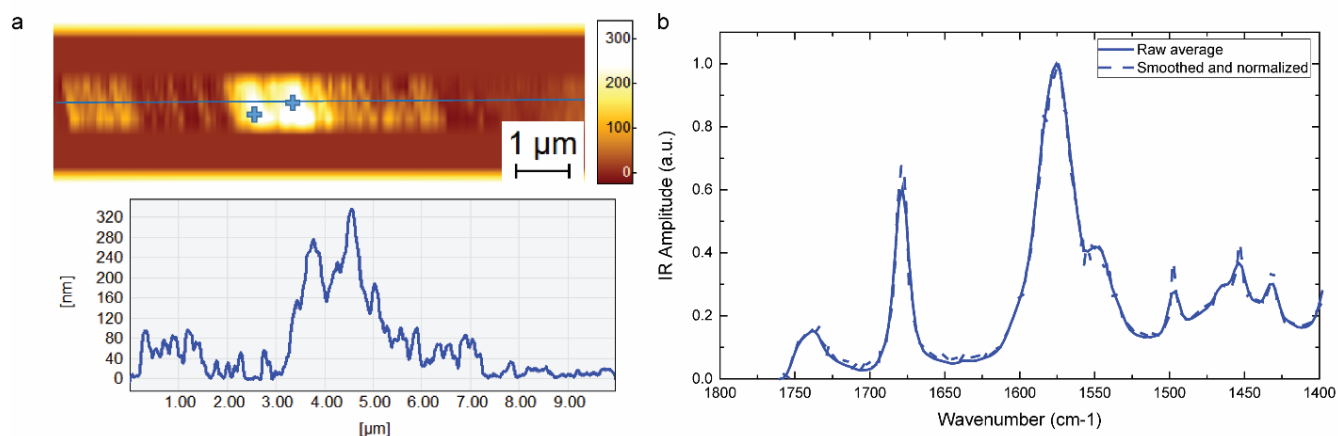


**Supplementary Figure 3. PTIR spectra of FF fibrils in H<sub>2</sub>O.** a) As recorded, b) averaged (dotted line) and smoothed (full line) PTIR absorption spectra of the FF fibril obtained in the position indicated by the red cross in Fig. 3b in water. c) Comparison of PTIR spectra obtained on a fibril and on the bare substrate. d) Spectrum obtained by dividing or subtracting the PTIR spectrum of FF with respect to the PTIR spectrum obtained on the substrate showing the typical spectral feature expected via literature comparison.<sup>47</sup> Average, smoothed and normalized spectrum of FF in H<sub>2</sub>O considering e) subtraction or f) division of the water

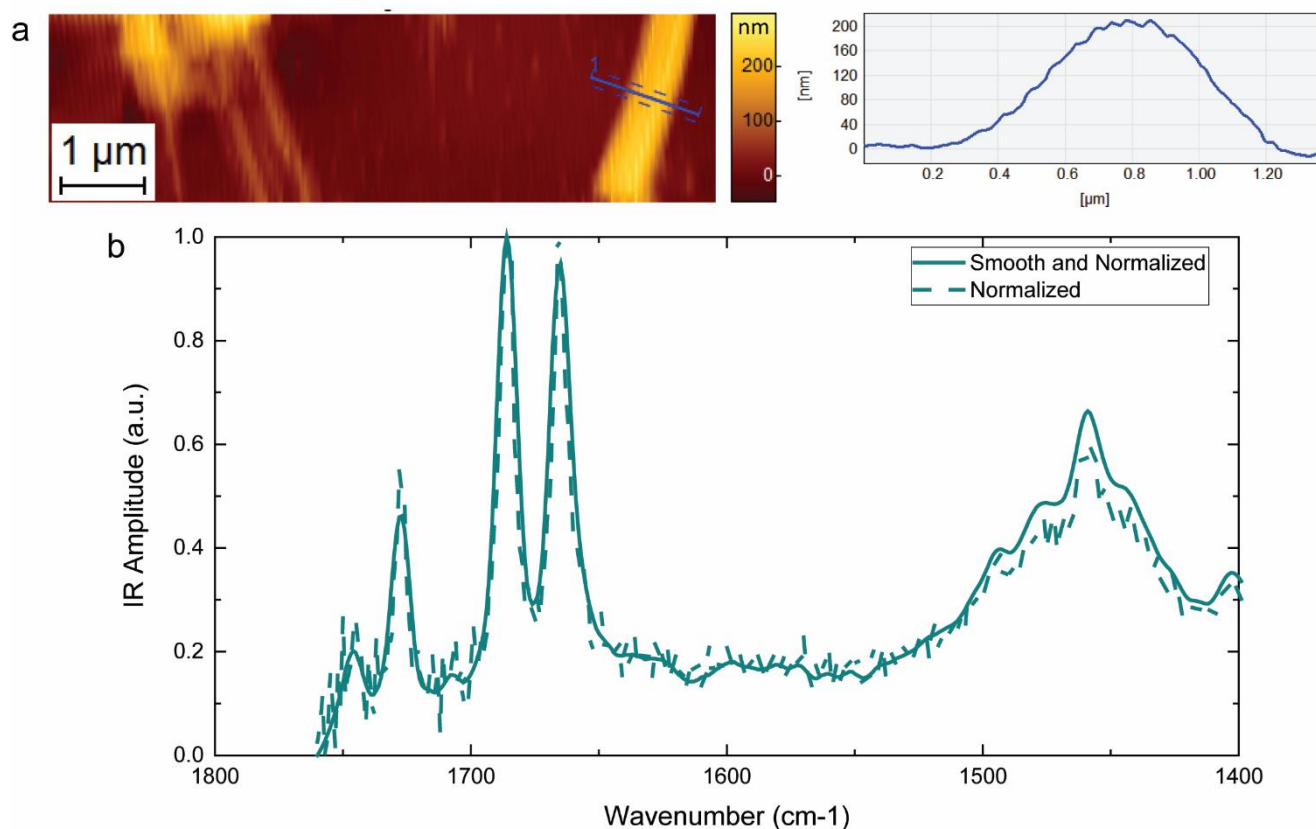
background as measured on the substrate. Because the PTIR signal is proportional to absorption, for our analysis in the main text, we used spectra obtained by subtracting the water absorption background.



**Supplementary Figure 4. Comparison of average PTIR spectra of FF fibrils in air, H<sub>2</sub>O and D<sub>2</sub>O.** a) Averaged and smoothed IR absorption spectra collected from the FF aggregates obtained in air (black), water (red) and D<sub>2</sub>O (blue). The spectra show high similarity. The amide band in the antiparallel  $\beta$ -sheet region shifts, as expected, to lower wavenumbers for the spectrum in D<sub>2</sub>O. Differences in the Amide band II arise from the differences in the protonation state in the different environment. b) Comparison of the second derivatives spectra in the region of the C-C ring absorption (orange region in panel a), demonstrating accurate chemical recognition.



**Supplementary Figure 5. Average PTIR spectrum of FF fibrils in D<sub>2</sub>O with 200-300 nm thickness.** a) AFM map of the FF aggregates in D<sub>2</sub>O. The blue + symbols mark the locations of spectra acquisition while the blue line marks the position of AFM height profile, which identify the fibril size (diameter). b) Averaged (dotted line) and smoothed (full line) PTIR absorption spectra.



**Supplementary Figure 6. PTIR spectra of Boc-FF fibrils in D<sub>2</sub>O.** a) AFM map of the Boc-FF aggregates in D<sub>2</sub>O their cross-sectional AFM height. b) Averaged (dotted line) and smoothed (full line) PTIR absorption spectra at the location indicated by the green cross in fig. 4a.